Supplemental Material: Temperature dependence of photoluminescence intensity and spin contrast in nitrogen-vacancy centers

S. Ernst[1,†], P. J. Scheidegger[1,†], S. Diesch[1], L. Lorenzelli[1], and C. L. Degen[1,2*]
[1] *Department of Physics, ETH Zurich, Otto Stern Weg 1, 8093 Zurich, Switzerland. and*
[2] *Quantum Center, ETH Zurich, 8093 Zurich, Switzerland.*
(Dated: June 22, 2023)

CONTENTS

I. Experimental 2

II. Measurements 3
A. PL vs. B 3
B. Time-resolved pulsed ODMR 3
C. Saturation measurement 4
D. Shelving state lifetime 4
E. Continuous time tagging 5

III. The numerical model 5
A. Level structure and optical transition rates 5
B. Orbital hopping rates 6
C. Master equation 6
D. Linking simulation with experiment 7
E. Evaluating sensing performance 8

IV. Data fitting and simulation 9
A. Calibration 9
B. Calibration results 10
C. Simulations and fits 12
D. Influence of the phonon model on our simulation 12

V. Additional simulations 14
A. Contrast, PL and sensitivty 14
B. Optimal integration time 14
C. Spin initialization and readout fidelity 14
D. Extrapolation to low strain or high magnetic field 14

VI. Spin mixing amplitudes 16

VII. Strain dependence of orbital hopping rates 17

References 17

I. EXPERIMENTAL

The majority of data presented in this work was acquired inside a dilution refrigerator (Setup A) on an isotopically pure (^{12}C) diamond sample doped with 7 keV NV centers in nanostructured pillars. To minimize heating by the microwave excitation, we employ an impedance-matched co-planar waveguide (CPW) made from thin-film aluminum on top of a sapphire substrate, which is identical to the CPW we used in our recent sub-Kelvin scanning magnetometry experiments [1]. To ensure good thermalization, we glue the diamond sample directly on top of the CPW, which in turn is glued on a sample holder made from copper. The sample holder contains both, a resistive heater and a calibrated thermometer (LakeShore Cernox). A PID controller is used to stabilize the temperature in a range from 4 K to 100 K with a temperature stability of 0.1K at low temperatures and $<$ 1K at very high temperatures. Towards higher measurement temperatures ($>$ 60 K), we increasingly find thermal drifts, which we stabilize by frequent optical tracking. Despite our efforts, one can observe that the contrast values measured in the high temperature limit are systematically lower than the simulated model (Fig. 1(b) and Fig. 3(e) of the main text). We attribute this to increased setup instabilities and possibly some uncertainty in the measured temperature, due to the large temperature gradient between the sample and the rest of the cryostat (Setup A).

For the optical excitation of the NV, we use a 520 nm diode-laser with home-built modulation circuitry. We characterize its rise time on fluorescent contamination in proximity to the NV center and obtain $\tau_R = 23 \pm 1$ ns . We calibrate the laser power directly at its output and use a conversion factor to fit the actual (lower) laser power on the NV. Heating of the diode slightly alters the output laser power, which is why we find a consistent mismatch by

a factor of 1.15 between the steady-state PL value in *time-resolved pulsed ODMR* and the *saturation* measurements (for details, see section II) and we scale our data accordingly.

We use a superconducting vector magnet (American Magnetics Inc.) to apply a magnetic field along the respective NV axis. The field is aligned by sweeping both spherical angles at a constant field magnitude of $B = 200\,\mathrm{mT}$ and minimizing the ODMR resonance of the $m_S = -1$ state . This calibration has been performed once for every NV. As common for superconducting magnets, we observe a remanent field of approximately 3 mT (projected onto the NV axis) after operation at elevated magnetic fields (here: 200 mT). We can reset the magnet by heating it to above the superconducting transition temperature and letting it cool down again. In our experiments, we perform such a reset when switching to a different NV (i.e. moving the magnetic field orientation) and when lowering the magnetic field magnitude. For measuring the PL as a function of magnetic field (c.f. II A), we sweep from high to low field while maintaining the same orientation (without resetting).

We note that our data was acquired over the course of three distinct cooldowns. In cooldown #1, we used a different microwave antenna than the CPW discussed above, which resulted in microwave heating. Consequently, we resorted to all-optical measurements of PL during this cooldown. Cooldowns #2 and #3 were identical in terms of experimental setup and used the aluminum CPW. All contrast vs temperature data on Setup A were taken during those cooldowns. During cooldown #2, two of our NVs (NV-2 and NV-4) bleached (i.e. they showed a complete loss of spin contrast at a reduced PL level). Bringing them to ambient conditions for a short time completely restored their previous properties and they have not shown signs of bleaching since. Importantly, all our data is consistent across all three cooldowns and in line with the observations in Setup B (NV-5), which emphasizes the independence of our results from setup-related conditions.

II. MEASUREMENTS

In our work, we use five types of experiments to thoroughly characterize each NV and to disentangle the various fitting parameters. Fitting the first three experiment types (II A - II C) is a simultaneous effort, further discussed in section IV A, due to shared parameters between all of them. The fourth experiment type, namely the the shelving state lifetime (II D), is determined independently. The fifth type of experiment (II E) is used to verify that we are working with the negative charge state NV^- of the NV center. This section discusses all five experiments in detail.

A. PL vs. B

We measure the steady-state PL while sweeping the magnitude of the magnetic field B from high field to low field (Fig. S1(a)). At base temperature, such a trace exhibits minima at the level anti-crossings (LAC) of the ES and the GS, which we use to uniquely characterize the in-plane strain and magnetic field alignment [2, 3].

While the relative depth of the ES LAC minima at base temperature (e.g. 30 mT and 55 mT in Fig. S1(a)) is known to depend on the ES branch-selectivity of the optical excitation [3], we find an additional dependence on the orbital hopping rate. Specifically, the spontaneous emission process $E_x \rightarrow E_y$ that is relevant in the presence of in-plane strain causes the first E_y LAC minimum to be deeper than the second E_x LAC minimum. The rate of this spontaneous emission process (c.f. Eq. S3) depends on the electron-phonon coupling strength η, which is a fit parameter in our model. To avoid cross-talk between the fit of η and the branch selectivity, we always assume no orbital branch selectivity in our optical excitation, i.e. $r_\beta = \beta_x/\beta_y = 1$ (c.f. Fig. S3). This assumption is reasonable for the following reasons: (i) we off-resonantly excite NV centers with green laser light into the phonon sideband, where the selectivity is naturally low even with aligned NV and laser polarization axes [4, 5]. (ii) our NV center principal axes are tilted by 55° relative to the diamond surface and optical axis, reducing the possible polarization alignment.

When fitting a *PL vs. B* measurement, we exclude points below 15 mT, to avoid possible distortions due to the remanent field of the vector magnet.

B. Time-resolved pulsed ODMR

We measure the time-resolved, spin state dependent PL under excitation with $\sim 2\,\mu\mathrm{s}$ laser pulses (Fig. S1(b)). After a such a laser pulse, the spin state of the NV center is initialized – with some laser power dependent fidelity [6] – into the $m_S = 0$ state. In a subsequent laser pulse, we thus obtain the time-resolved PL of the $m_S = 0$ initialized state.

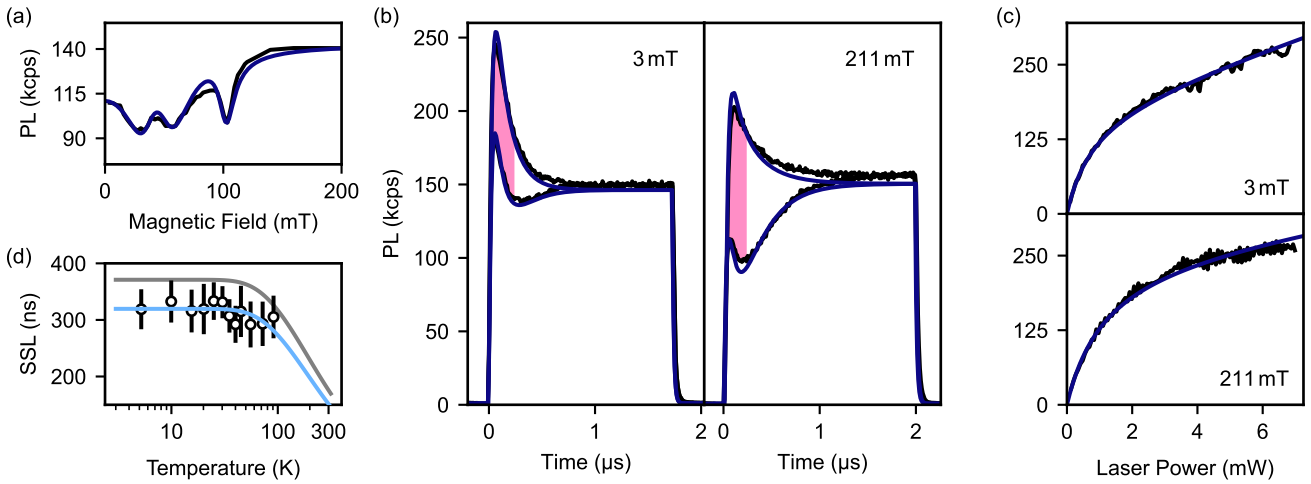

Figure S1. **Example for measurement types used in our fitting process** - Shown are complementary measurements used in this work, with their corresponding fits (solid blue lines), taken on NV-2. (a - c) were taken at base temperature ($\sim 5\,\mathrm{K}$) and constitute a typical data set for the simultaneous fitting described in section IV A. (a) *PL vs. B* measurement. (b) *Time-resolved pulsed ODMR* at low and high magnetic field. Contrast is integrated over the pink shaded area (first 250 ns). (c) *Saturation* measurement. (d) Measurement and fit of the temperature dependence of the SSL. For comparison, the findings of Robledo *et al.* [7] are also shown (grey).

Likewise, if a microwave pulse that results in an adiabatic inversion of the spin state is applied beforehand, we obtain the time-resolved PL of the $m_S = -1$ initialized state. The relative difference between these two traces, integrated over the first 250 ns, results in the ODMR spin contrast. Explicitly, the contrast is calculated from the integrated counts of the $m_S = -1$ state divided by the integrated counts of the $m_S = 0$ state. We find that the contrast is fairly resilient against changes in setup-specific parameters. In addition to determining contrast, we use the raw, time-resolved PL traces to fit for the rates related to the optical lifetime and intersysten-crossing (ISC) process. We note that setup-specific parameters also change the curve shape.

C. Saturation measurement

The measurement of the steady-state PL while sweeping the laser power shows a characteristic saturation behavior that arises when the optical excitation rate exceeds the lifetime of the electronic excited state. Then, the laser power dependent PL becomes linear with a slope given by the fluorescent background (c.f. Fig. S1(c)). The laser power at which the saturation is reached is characteristic for the excitation efficiency. The absolute PL level on the other hand is characteristic for the collection efficiency. Therefore, saturation measurements are primarily suited to characterize these three setup-specific parameters (background, excitation and collection efficiency) and to disentangle them from rate parameters.

D. Shelving state lifetime

The shelving state lifetime (SSL), i.e. the time spent in the intermediate singlet levels before decaying back into the GS (c.f. Fig. 2 of the main text), has a well-known temperature dependence that we include in our model of the NV photo-physics. We measure the SSL following Refs. [7, 8], by first exciting the NV into the shelving state using a $1.2\,\mu$s laser pulse and subsequently probing the initial PL in a second laser pulse, delayed by τ. The resulting exponential rise PL $\propto 1 - ae^{-\tau/\tau_S(T)}$ can be fitted for the SSL $\tau_S(T)$ at the measurement temperature T. Obtaining such data points $\tau_S(T)$ for several temperatures allows in a second step to fit the parameters of the temperature dependence of the SSL. We fit $\tau_{S,0}$ at zero temperature from Eq. S1 for each NV center individually. The fit results are given in table I. Fitting $\tau_S(T)$ reliably for ΔE in Eq. S1 requires a significant amount of measurements in the range $T \gg 100\,\mathrm{K}$, which was not accessible in our experiments. We therefore use the same $\Delta E = 16.6\,\mathrm{meV}$ as reported by Robledo *et al.* [7]. In Fig. S1(d) we present the result of such an evaluation scheme at the example of NV-2.

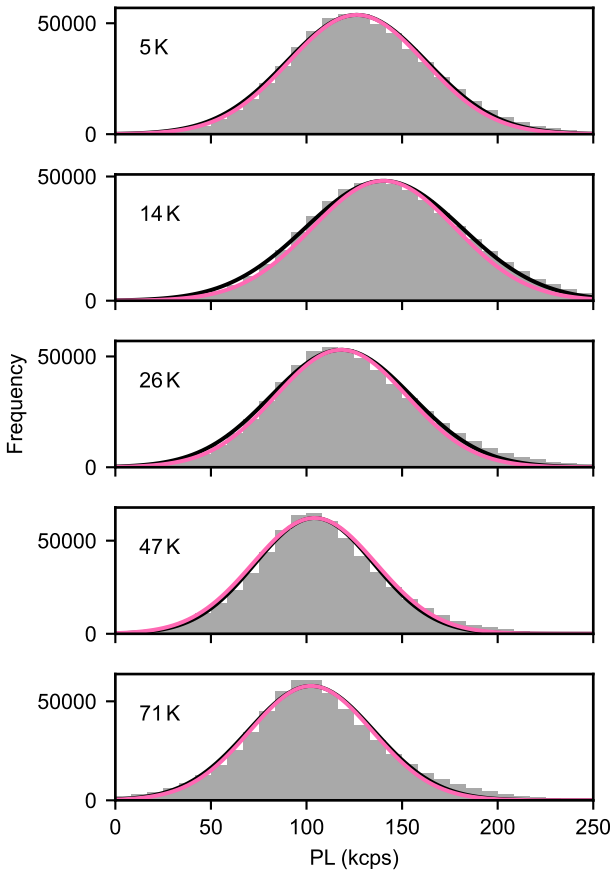

Figure S2. **Histograms of the PL count rate of NV-1 at varying temperatures** - Dilution refrigerator vibrations at 1.4 Hz and 140 Hz and their harmonics have been removed from the data. The pink curve indicates the theoretical shot noise limit of the measurement, the black line is a Gaussian fit to the histogram.

E. Continuous time tagging

At each temperature step, after all other measurements are completed, we additionally record PL during 60 s of continuous laser illumination. The raw timetags (resolution: 10 ns) are binned with a sampling rate of 10 kHz to obtain count-rate histograms as shown in Fig. S2 (for NV-1 at select temperatures). After removing noise from pulse tube vibrations (1.4 Hz) and rotary valve motor vibrations (140 Hz) and their harmonics, the histograms approximate the shot noise limit well. The strictly Gaussian nature of the signal indicates that no blinking occurred on our NVs on time scales limited by the 60 s-long measurement time on slow time-scales, and the 10 kHz sampling rate on fast time-scales. This supports our conclusion in the main text, that charge-state switching between NV^- and NV^0 is not involved in the temperature-dependent reduction of PL and contrast.

III. THE NUMERICAL MODEL

Our model is derived in detail in Ref. [9]. Here, we summarize the most important equations and relate them to our fitting algorithm.

A. Level structure and optical transition rates

We calculate the NVs energy level structure and eigenstates at a given magnetic bias field (with magnitude B, polar angle θ_B and azimuthal angle ϕ_B) and in-plane strain (with magnitude $\delta_\perp$ and azimuthal angle ϕ_δ) using the

well-established low temperature Hamiltonian [10]. We neglect the hyperfine interactions and on-axis strain, as they are not relevant for this work. Angles are measured relative to the NV coordinate system in Ref. [10]. Between the calculated levels, we define transition rates to model optical excitation ($\beta_{x/y}k_r$) and relaxation (k_r, $k_{E_{12}}$, $k_{E_{xy}}$, k_{A_1}), as well as phonon-mediated spin-conserving transitions ($k_{\uparrow/\downarrow}$), as depicted in Fig. S3. To do so, it is convenient to implement the Hamiltonian in different bases and transform between them.

We assume no temperature dependence for the optical excitation k_r [11]. The intersystem-crossing (ISC) transitions from the excited state to the shelving state (SS) have been shown to be slightly temperature dependent [12, 13] at high temperature, but the effect is too small to have an impact on our model. The temperature dependence of the ISC rates below 30 K, as reported in their work, is readily contained in our model [9].

The SS relaxation, on the other hand, has a well established temperature dependence and we model it following Robledo *et al.* [7]

$$\tau_S(T) = \frac{1}{k_{S0} + k_{S1}} = \tau_{S,0}\left(1 - e^{-\frac{\Delta E}{k_B T}}\right) \tag{S1}$$

with a spontaneous emission process ($\tau_{S,0}$) and a stimulated emission process of a phonon with energy ΔE. Here, k_B is the Boltzmann constant and we use the literature values for ΔE (see table I). We note that the branching ratio $r_S = k_{S0}/k_{S1}$ remains approximately constant in temperature [14].

B. Orbital hopping rates

The primary effect of temperature in our model lies in the addition of hopping rates between the two orbital branches to the rate model, similar to previous studies [4, 12, 15]. This hopping is caused by one- and two-phonon-processes and thus depends on the thermal occupation of phonon modes. We introduce rates

$$\begin{aligned} \mathrm{E_y} \to \mathrm{E_x} : k_\uparrow(T, \delta_\perp, \eta) = k_{\uparrow,1} + k_{\uparrow,2} \\ \mathrm{E_x} \to \mathrm{E_y} : k_\downarrow(T, \delta_\perp, \eta) = k_{\downarrow,1} + k_{\downarrow,2} \end{aligned} \tag{S2}$$

which depend on both temperature T and the strain induced splitting of the orbital branches, which is approximately $\approx 2\delta_\perp$ for a sufficiently small $g_l B_z$, as we expect for all our measurements [3]. The coupling strength between electronic orbital states of the NV^- and phonons is given by η.

The expressions for the hopping rates can be derived following Fermi's Golden Rule, as is done in Refs. [9, 15, 16]. Here, we just state the results. For the one-phonon process, one finds

$$\begin{aligned} k_{\uparrow,1}(T, \delta_\perp) &\approx 32\eta h^3 \delta_\perp^3 n(2\delta_\perp h) \\ k_{\downarrow,1}(T, \delta_\perp) &\approx 32\eta h^3 \delta_\perp^3 \left[n(2\delta_\perp h) + 1\right] , \end{aligned} \tag{S3}$$

where the Bose–Einstein distribution $n(\epsilon)$ describes the thermal occupation of phonon modes with energy ϵ at temperature T. The rates for the opposite directions are related by detailed balance as $k_\uparrow = \exp\left(-\frac{2\delta_\perp h}{k_B T}\right) k_\downarrow$. Notably, the spontaneous emission term ("+1") in $k_{\downarrow,1}$ results in a finite, strain-dependent rate that needs to be considered even at $T = 0$ K.

For the two-phonon process, we find

$$\begin{aligned} k_{\uparrow,2}(T, \delta_\perp) =& \frac{64\hbar}{\pi}\eta^2 k_B^5 T^5 \int_{x_\perp}^{\Omega/k_B T} \frac{e^x x(x - x_\perp)\left[x^2 + (x - x_\perp)^2\right]}{2\left(e^x - 1\right)\left(e^{x - x_\perp} - 1\right)} dx \\ =& \frac{64\hbar}{\pi}\eta^2 k_B^5 T^5 I(T, \delta_\perp) , \end{aligned} \tag{S4}$$

where x is the phonon energy in units of $k_B T$ and $x_\perp \approx \frac{2\delta_\perp h}{k_B T}$. In the second line, we introduced the temperature- and strain-dependent integral over the phonon modes $I(T, \delta_\perp)$. Using the detailed balance, one can directly obtain $k_{\downarrow,2}(T, \delta_\perp)$.

C. Master equation

Importantly, the orbital hopping rates $k_{\uparrow/\downarrow}$ only act on the orbital subspace, leaving the state in the spin subspace untouched. This cannot be modeled by a classical rate equation model as is commonly used. We therefore employ

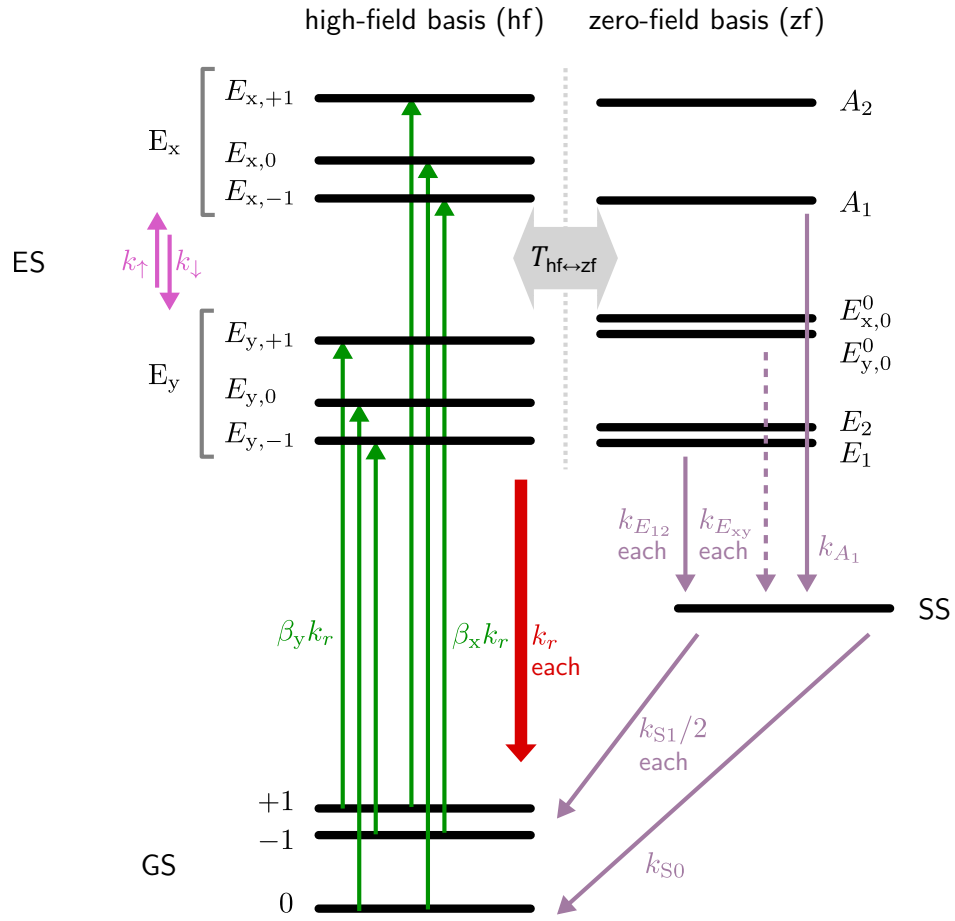

Figure S3. **Energy levels and transition rates** - Depicted are the 10 energy levels of the zero-temperature NV^- center Hamiltonian. The ES is depicted in two different bases: the high-field basis (hf) which is a good eigenbasis at high magnetic field $\vec{B} \parallel \hat{e}_z$ and high strain $\delta_\perp$ and the zero-field basis (zf), which covers the limit of $\vec{B} \to 0$ and $\delta_\perp \to 0$. Transition rates (arrows) are implemented in the basis in which they are defined and we use basis transformations to combine them into a single master equation (c.f. section III C). Optical excitation ($\beta_{x/y} k_r$) from the ground state GS to the two branches (E_x, E_y) of the excited state ES is spin m_s conserving and dependent on the excitation power and polarization (x, y). Optical decay (k_r) is also spin conserving and leads to the emission of a red photon. The ISC rates ($k_{E_{12}}$, $k_{E_{xy}}$, k_{A_1}) are dependent on the fine structure levels, which are good eigenstates in zero-field. The decay from the SS to the GS repopulates all spin states, with a branching ratio defined as $r_S = k_0/k_{S1}$. Phonon mediated, coherent spin state preserving transitions ($k_{\uparrow/\downarrow}$) between the two orbital branches occur at a rate that increases with temperature.

a master equation model that acts on quantum states but can include the known classical rates via jump operators. We numerically calculate the time evolution of the 10-dimensional density matrix ρ (including the three GS states, six ES states and the SS) using the Liouville equation

$$\frac{\mathrm{d}}{\mathrm{d}t}\hat{\rho} = -\frac{i}{\hbar}\left[\hat{H}, \hat{\rho}\right] + \sum_k \left(\hat{L}_k \hat{\rho} \hat{L}_k^\dagger - \frac{1}{2}\left\{\hat{L}_k^\dagger \hat{L}_k, \hat{\rho}\right\}\right) \equiv \mathcal{L}(\rho)\,. \tag{S5}$$

Details on the implementation of the jump operators can be found in Ref. [9].

D. Linking simulation with experiment

The quantity we observe in our experiments is always the PL averaged over some time or many repetitions of a sequence of laser and microwave pulses. The PL is composed of radiative emission of the NV^- center and fluorescent background radiation. We assume a linear dependence of the background PL on the laser power. The collected PL can be calculated from the populations $\rho_{i,i}$ of the emitting levels, which have the same indices $i \in [4, 9]$ for all bases.

We thus model the observed PL as:

$$\mathrm{PL}(t) = AR\left(\sum_{i\in[4,9]} \rho_{i,i}(t)k_r\right) + bP \tag{S6}$$

where we introduce a set of setup-related parameters. A represents the optical excitation efficiency (unit: W^{-1}), which can drift over time and change from experiment to experiment if setup conditions are not stable enough. R is the ratio of collection over excitation efficiency (unit: cps W s) and is expected to be fairly stable against drifts in the optical path. Lastly, b characterizes the background counts (unit: cps W), which are linear in the laser power P.

To simulate and fit the time-resolved PL response of NV centers in our setup as given in Fig. 1(a) of the main text, we need to take the rise time of our laser pulses into account. Thus, we introduce the laser rise time τ_R to our model, the value of which we determined experimentally. This is necessary when fitting $\mathrm{PL}(t)$ time traces as τ_R of our laser is longer than the time resolution of our photo-detector (10 ns). In the derivation of our model we assume a time-independent Liouvillian superoperator $\mathcal{L}$ in the Liouville equation S5. The laser power P enters into $\mathcal{L}$ in the form of a pre-factor of the jump operators describing the optical excitation. We thus need to ramp up the laser power and thus $\mathcal{L}$ in N discrete steps

$$P(t) = \begin{cases} 0 \text{ if } t < t_0 \\ P\left(1 - e^{\frac{t_n}{\tau_R}}\right) \text{ for } t_n = \left\lceil \frac{t-t_0}{\Delta t} \right\rceil \Delta t \\ P \text{ if } t > t_0 + N\tau_R \end{cases} \tag{S7}$$

and use fix parameters $N = 4$ and $\Delta t = 5\,\mathrm{ns}$ here. We find that the influence of τ_R on the spin contrast is negligibly small. In fitting time-resolved pulsed ODMR traces, on the other hand, τ_R is crucial. Likewise, we need to determine the precise value of t_0 individually for each measurement. This is done by a linear extrapolation to $\mathrm{PL} = 0$ from the first two data points above the dark count level, which we also determine and include in the model.

E. Evaluating sensing performance

In this work, we aim to give a direct comparison of the performance of the NV^- center as a sensor over a vast range of parameters. To that end, it is necessary to compare the optimized performance for each parameter setting, as done in section V A. We optimize the integration time of simulated pulsed ODMR experiments, which are representative for all kinds of sensing schemes. We note though, that also the laser power could be optimized, which is beyond the scope of this work. In the following, we give a brief derivation of the sensitivity and its relation to the SNR.

We assume a pulsed ODMR experiment to measure the magnetic field component along the NV axis [17]. The sensitivity $s = \Delta B_{\min}\sqrt{t}$ is then given by the minimal magnetic field change $\Delta B_{\min}$, that can be measured within time t. The microwave frequency f dependent photon counts signal $\mathcal{S}$ has the shape of a Gaussian with

$$\mathcal{S}(f) = \left[1 - e^{-4\ln(2)(f-f_0)^2/\nu^2}\right]\mathcal{S}_{m_\mathrm{S}=0}\,,$$

where f_0 is the resonance frequency at which a pi-pulse between the spin levels can happen, and ν is the full width half maximum (FWHM) of the Gaussian (and related to the inverse spin coherence time). The $\mathcal{S}$ ($\mathcal{S}_{m_\mathrm{S}=0}$) are the total collected counts during t that fall into the integration window t_int with (without) a microwave pulse applied before the laser pulse (c.f. Fig. S1(b)). Since f_0 shifts with the magnetic field as $\Delta B = \Delta f\, 2\pi/\gamma = \Delta f/28.025\,\mathrm{MHz\,mT^{-1}}$, best (i.e. smallest) sensitivity is achieved at the frequency f_s of highest slope of $\mathcal{S}(f)$. At this frequency, a pulsed ODMR experiment is performed, repetitively consisting of a pi pulse and a subsequent laser pulse for readout and re-initialization. Assuming a shot noise $\Delta\mathcal{S} = \sqrt{\mathcal{S}}$ limited readout at f_s, one finds for the sensitivity

$$s = \frac{2\pi}{\gamma} m_G^{-1} \frac{\nu\sqrt{r_G}}{C\sqrt{\mathrm{PL}_{m_\mathrm{S}=0}}\sqrt{\mathrm{DC}}}\,. \tag{S8}$$

Due to the Gaussian shape, $m_G^{-1} = 0.700$ and $r_G = 1 - 0.607\cdot C$. Further, $\mathrm{PL}_{m_\mathrm{S}=0} = \mathcal{S}_{m_\mathrm{S}=0}/(t_\mathrm{int}N_\mathrm{seq})$ is the average PL count rate during t_int, with $N_\mathrm{seq} = t/T_\mathrm{seq}$ the number of repetitions of the pulsed ODMR sequence of duration T_seq. Finally, the readout duty cycle $\mathrm{DC} = t_\mathrm{int}/T_\mathrm{seq}$ and the spin contrast $C = 1 - \mathcal{S}(f_0)/\mathcal{S}_{m_\mathrm{S}=0}$.

Viewing the readout of the spin state in a generalized and ideal scheme [18] a similar result of

$$s \propto \mathrm{SNR}^{-1} \propto \frac{\sqrt{r}}{C\sqrt{\mathrm{PL}_{m_\mathrm{S}=0}}} \tag{S9}$$

can be found for the sensitivity and SNR. Here, $r = 1 - 0.5 \cdot C$.

In simulations with optimal readout, we optimize Eq. S8 at every parameter setting for the t_int that gives best sensitivity. Explicitly, this yields not the t_int with highest contrast. For a more intuitive picture, the inverse sensitivity and SNR are approximately proportional to

$$\mathrm{SNR} \sim C\sqrt{\mathrm{PL}_\mathrm{ss}}\,, \tag{S10}$$

with the quantities spin contrast C and steady-state PL (here called PL_ss for clarity) used elsewhere in this work.

IV. DATA FITTING AND SIMULATION

In this section, we describe how we fit our measurements to calibrate the model and then, subsequently, simulate the NV PL to compare the theory to our measurements. When fitting, we distinguish two primary sets of fit parameters. The first set, the *robust* parameters, includes all NV-intrinsic parameters (i.e. strain and rates) and the magnetic bias field, which we have good control over. These parameters are stable against scanning stage movements and other drifts which can occur between measurements, particularly when changing to a new temperature or magnetic field. The second set, the *environment-sensitive* parameters, is prone to change between measurements. They include the setup parameters discussed in section III D. These definitions help to distinguish the following three processes:

- *Calibration*: Simultaneous fit of multiple data sets across multiple temperatures T_i and fields B_i with common *robust* parameters but unique *environment-sensitive* parameters for each T_i/B_i. The procedure is described in great detail in the next section IV A.
- *Simulation*: Uses the calibration-results for the *robust* parameters and a *single* set of *environment-sensitive* parameters to effectively extrapolate the NV photo-physics to the full range of temperature, magnetic field and strain. This is used, for example, in contrast vs. temperature curves (c.f. Fig. 1(b) in the main text) and in maps of PL vs. B vs. T (c.f. Fig. 3(a)). Deviations from experimental data are found, particularly at high temperatures where drifts become significant.
- *Fits*: Fits use the calibration-results for the *robust* parameters but exclusively re-fit the *environment-sensitive* parameters to a given data set at a specific (T, B). This effectively corrects for experimental drifts. Examples are fits of *PL vs. B* (c.f. Fig. 3(b)) measurements and PL traces (c.f. Fig. 1(a)).

A. Calibration

The NV center Hamiltonian that we use in our model contains eight fundamental constants describing the various interactions that yield its spin and electronic eigenstates at zero temperature. We use recent literature values for these [2, 10, 19, 20] and assume them to be the same for all conditions. Apart from those constants, there are several other parameters in the model: (i) NV center specific crystal strain parameters, (ii) magnetic bias field related parameters, (iii) rates, (iv) electron-phonon interaction, and finally (v) setup specific parameters. A subset of those parameters is fixed during the complete calibration process described below, either because they are *predetermined* from separate measurements (e.g. laser rise time) or because they are taken from literature. An overview of all parameters (fitted and fixed) and their respective categorization (robust, environment-sensitive, predetermined, literature) is given in Tab. I.

We perform the fitting in three stages (I-III), where each stage informs the set of initial parameters of the subsequent fit. This ensures good convergence despite the vast number of parameters.

(I) We start by fitting a *PL vs. B* measurement at base temperature ($\sim$ 5K) to our full model. We fit for the in-plane strain ($\delta_\perp$, ϕ_δ) and magnetic field alignment (θ_B, ϕ_B) as well as the setup-specific parameters (b, R, A). We use common literature values for all other parameters.

(II) We then simultaneously fit a data set consisting of five different measurements at base temperature, with all parameters being fitted (except for η). This data set includes (i) the *PL vs. B* from before, (ii) two *time-resolved*

		NV-1	NV-2	NV-3	NV-4	
Strain						
$\delta_\perp$	ES in-plane strain (GHz)	31.8	39.9	8.7	80.2	*a*
ϕ_δ	ES in-plane strain angle	39.9°	24.4°	0.8°	59.9°	*a*
Magnetic bias field						
θ_B	mag. field alignment angle	1.7°	1.9°	1.8°	2.2°	*a*
ϕ_B	mag. field in-plane angle	244.0°	17.6°	106.5°	130.6°	*a*
ϕ_B	cooldown #1	256.2°	194.2°			*a*
Rates						
k_r	opt. emission rate (μs^{-1})	55.1	55.7	45.3	40.5	*a*
$k_{E_{12}}$	ISC rate from $E_{1,2}$ (μs^{-1})	112.4	98.7	101.3	90.7	*a*
k_{A1}	ISC rate from A_1 (μs^{-1})		$k_{E_{12}}/0.52$ [12]			*d*
$k_{E_{xy}}$	ISC rate from $E_{x,y}$ (μs^{-1})	9.1	8.2	8.6	7.5	*a*
$r_\beta = \beta_x/\beta_y$	opt. exc. branching ratio		1			*c*
$r_S = k_{S0}/k_{S1}$	SS branching ratio	1.36	2.26	1.44	1.15	*a*
$\tau_{S,0} = 1/(k_{S0}+k_{S1})$	SS decay time at $T = 0\,K$ (ns)	342	320	292	318	*c*
ΔE	SS emit. phonon energy (meV)		16.6 [7]			*d*
Electron-phonon interaction						
η	ES coupling strength ($\mu s^{-1}\,meV^{-3}$)	197	176	268	249	*a*
Ω	phon. cutoff energy (meV)		168			*d*
Setup - Base temperature PL vs. B measurement						
b	background (kcps mW^{-1})	40.8	27.5	52.6	34.7	*b*
R	$\frac{\text{collection}}{\text{excitation}}$ efficiency (kcps mW µs)	67.1	88.4	112.1	178.3	*b*
A	opt. alignment (W^{-1})	245.1	136.2	282.3	188.1	*b*
τ_R	laser rise time (ns)		23			*c*

Table I. **Calibration results per NV center** - We fit the NV center intrinsic parameters individually for each center since they are known to vary between NV centers [10]. The fit results for setup related parameters of saturation and time-resolved pulsed ODMR measurements of the same simultaneous fits are presented in Fig. S4. The last column specifies the type of parameter: (a) robust parameters, including NV intrinsic properties and the well-controlled magnetic bias field; (b) environment-sensitive parameters, which include optical excitation and collection efficiencies; (c) pre-determined parameters; (d) literature values (Hamiltonian parameters not shown). The latter two (c, d) are fixed when fitting for (a) and (b).

pulsed ODMR traces and (iii) two *saturation* measurements at low (3 mT) and at high (200 mT) magnetic field. Such a data set for NV-2 is shown in Fig. S1.

(III) Finally, we fit the same base-temperature *PL vs.* B together with 6 (5 for NV-4) pairs of *time-resolved pulsed ODMR* and *saturation* measurements, sampled across our full temperature range. This allows us to fit for the electron-phonon coupling strength η, in addition to a final fine-tuning of the full parameter set. Crucially, we use a common set of *robust* parameters across all data sets, but individual *environment-sensitive* parameters are used for each data set, which account for mechanical drifts in the experimental setup. Specifically, the two parameters background b and collection over excitation ratio R are fitted separately to each pair of *saturation* and *time-resolved pulsed ODMR* measurements (at the same field and temperature) and also separately to the base-temperature *PL vs.* B measurement. Further, the alignment parameter A has to be fitted separately for every single measurement. This results in a total of 60 fit parameters simultaneously fitted to 25 distinct measurements.

We find that the simultaneous fit of these 25 measurements in stage (III) improves the stability of the fit compared to stage (II) containing only the five base temperature measurements. Particularly, the in-plane magnetic field angle, which results from finite misalignment, can have little observable effect on the PL at base temperature but plays a more significant role at higher temperature.

B. Calibration results

Results of the calibration for the different NV centers are presented in Tab. I and Fig. S4. The latter contains the *environment-sensitive* parameters that have been determined across all temperatures, as described above. For NV-1 we were not able to include *saturation* measurements in the fit as the PL stability required here was not sufficient. We stress that the fitted setup-parameters do not show a correlation with temperature. In particular, in Fig. S4 we

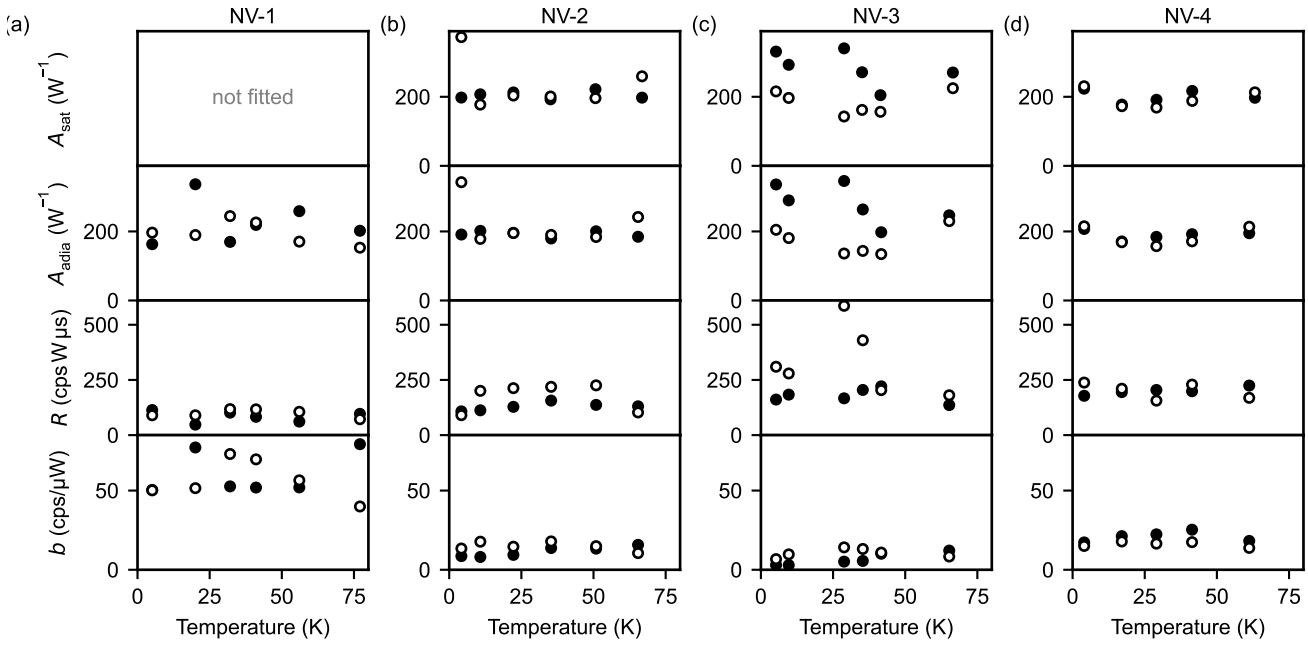

Figure S4. **Calibration results for the *environment-sensitive* parameters per NV center** - Shown are the results for the *saturation* ("sat") measurements and *time-resolved pulsed ODMRs* ("adia") at low (3 mT, empty ciclres) and at high (200 mT, filled circles) magnetic field. Temperature-independent results of the same calibration per NV center are given in Tab. I. Shown here are the optical alignment A, the ratio of collection over excitation efficiency R (common to both "sat" and "adia") and background b (also common to both).

Reference	SS branching ratio r_S
this work	1.15 – 2.26
Tetienne *et al.* [21]	0.0 – 1.9 †
Robledo *et al.* [7]	1.1 – 2.0
Gupta *et al.* [22]	2.0 – 2.3
Kalb *et al.* [23]	2.0 – 8.0 †
Wirtitsch *et al.* [6]	13.3

Reference	ES coupling strength η (µs^{-1} meV^{-3})
this work	176 – 249
Plakhotnik *et al.* [15]	144
Abtew *et al.* [24]	149
Goldman *et al.* [12]	276

Table II. **Comparison to literature values** - Our calibrated values of r_S (left) and η (right) are compared to measurement values from other studies. For each study, we give the maximum parameter range (where applicable), considering measurement error and measurements on multiple NVs. Values denoted with † were transformed from a 7-level system convention to the 5-level system used in this work.

do not see any feature at ~ 30 K, the location of the contrast and PL minimum.

Since cooldown #1 has different magnetic field alignment due to changes in the setup, a different in-plane magnetic field angle was used for the *PL vs. B* measurement at base temperature if fitted simultaneously with measurements from cooldown #2 and #3 – this is the case for NV-2 and NV-1. Based on our measurements, we can only determine the in-plane magnetic field and strain angle relative to one out of three possible crystal axes, which we then call the x-Axis of our coordinate system [10]. Moreover, we do not know the sign of the z-Axis. Therefore, given the three-fold rotational symmetry and mirror symmetry to the xz-plane, we choose to determine values for the in-plane strain angle in the range $[0°, 60°]$. The in-plane magnetic field angle can then have any orientation relative to it, i.e. covers a range of $[0°, 360°]$.

We compare the calibration results of select parameters to literature values in table II. First, we note that our SS branching ratio r_S fits well into the broad range of values obtained in other experiments. It appears that r_S varies substantially between NV centers even within individual studies. Theoretical modelling prefers a higher $r_S \approx 6$ [14] than measured in many of those works, including ours. The cause for this disparity is unknown, and no significant strain or temperature dependence has been observed to date. This represents an open question that will have to be addressed with suitable measurement techniques in future work.

Second, our measured electron-phonon coupling strength η falls right into the already established parameter range in literature, validating our measurement approach.

C. Simulations and fits

From the fitting process described above, we obtain all quantities needed to model the PL and contrast of each NV center in dependence of temperature, magnetic field, and strain. When performing these simulations, we fix the *environment-sensitive* parameters to values obtained at base temperature. For *PL vs. B*, these are the values given at the bottom of table I. For contrast simulations, we use the lowest-temperature values in Fig. S4 at the respective magnetic field. Based on this set of parameters, we perform simulations of PL and contrast at all temperatures.

For *PL vs. B*, this process results in the maps shown in Fig. 3(a) in the main text for NV-1 and Fig. S5(a-c) for all other NVs. The maps emphasize the rich strain-dependence of the PL. We also note that when comparing the similarly-strained NV-1 and NV-2 (Fig. S5(b)), we predict a feature in the form of a small peak at $\sim 50\,\mathrm{mT}$ and $\sim 50\,\mathrm{K}$ in the map of NV-2 which arises due to a different in-plane strain angle ϕ_δ [9].

We performed *PL vs. B* measurements at select temperatures covering all three regimes (I-III) discussed in the main text, which we can compare with the theory by only refitting the *environment-sensitive* parameters b and R, while otherwise using results of the calibration. This has approximately the same effect as defining a scaling and an offset on our PL data and thus corrects for setup drifts. We find good agreement between measurement and fits for all NVs (Fig. 3(b) of the main text and Fig. S5(d-f)). We were, however, not able to resolve some small features such as the peak predicted for NV-2, likely due to a combination of remanent field effects, drift in setup parameters during one sweep, and pulse-tube vibration noise limiting our resolution of PL. We assumed the same magnetic field alignment for all measurements, i.e. we exclusively use the magnetic field orientation from the calibration fit. However, some drift and/or hysteresis of the vector magnet becomes apparent from the mismatch between data and fit in the width of the dips at the the ground state LAC ($\sim 100\,\mathrm{mT}$) in Fig. S5(d).

To perform simulations of contrast versus temperature, we simulate and evaluate *time-resolved pulsed ODMR* sequences at the desired temperatures. In the main text, we find a good match between our simulation and the measurement data, despite the fact that the simulation uses fixed *environment-sensitive* parameters, whilst we find significant variation in the calibration at different temperatures (Fig. S4). This emphasizes the great stability of contrast measurements against setup drifts.

Finally, for Fig. 1(a) of the main text we use the parameters of the calibration and only (re-)fit the *environment-sensitive* parameters of the time-resolved pulsed ODMR traces shown in Fig. 1(a) together with their respective saturation measurement (with shared b and R and individual A as done in the calibration above).

D. Influence of the phonon model on our simulation

As mentioned in the main text, the temperature dependence of the orbital hopping rate is still under debate [14]. In Ref. [9] we give a detailed discussion of the usage of our model as a novel tool to investigate the nature of contributing phonon modes. Here, we aim to put our findings in context with previous studies.

We have already found good agreement of our fitted electron-phonon coupling strength η with literature values (c.f. Table II). However, we note that in all of these studies, different assumptions about the contributing phonon modes where made. In particular, the integral over the phonon spectrum $I(T)$ for the two-phonon process (c.f. Eq. 2 of the main text or Eq. S4 here) was in all cases solved in the Debye approximation but with a different phonon cut-off energy Ω. In this work, we assumed the Debye temperature of diamond ($\Omega_\mathrm{D} = 168\,\mathrm{meV}$) as the cut-off energy. But in a study by Plakhotnik *et al.* [15], a much lower value of $\Omega_\mathrm{P} = 13.4\,\mathrm{meV}$ was found.

To investigate the effect of such a low cut-off energy, we use the value of Ω_P in our model and repeat the calibration of section IV A. As expected, it significantly alters the model, yielding higher fit results of η (NV-2: $284\,\mu\mathrm{s}^{-1}\,\mathrm{meV}^{-3}$, NV-3: $512\,\mu\mathrm{s}^{-1}\,\mathrm{meV}^{-3}$, NV-4: $427\,\mu\mathrm{s}^{-1}\,\mathrm{meV}^{-3}$) and a slower recovery towards room temperature. Comparing the fits in Fig. S6, we find that using Ω_D yields better results at low temperatures and high magnetic fields, while – due to the slower recovery – Ω_P matches the high temperature data slightly better. Thus, presumably due to the setup instabilities and uncertainty in temperature calibration at high temperatures in Setup A (see section I), the data presented in this work does not allow to definitely rule out either of the models. In the main text we exclusively present data fitted with Ω_D, since the overall match appears better and the fitted coupling constant η agrees well with literature values. We did not attempt to fit Ω in this work and expect that the correct phonon spectrum has to be used rather than a Debye model with fitted cutoff energy Ω. For future experiments, we expect a more stable contrast versus temperature measurement in the range 80 K to 150 K to give valuable insight into the contributing phonon modes.

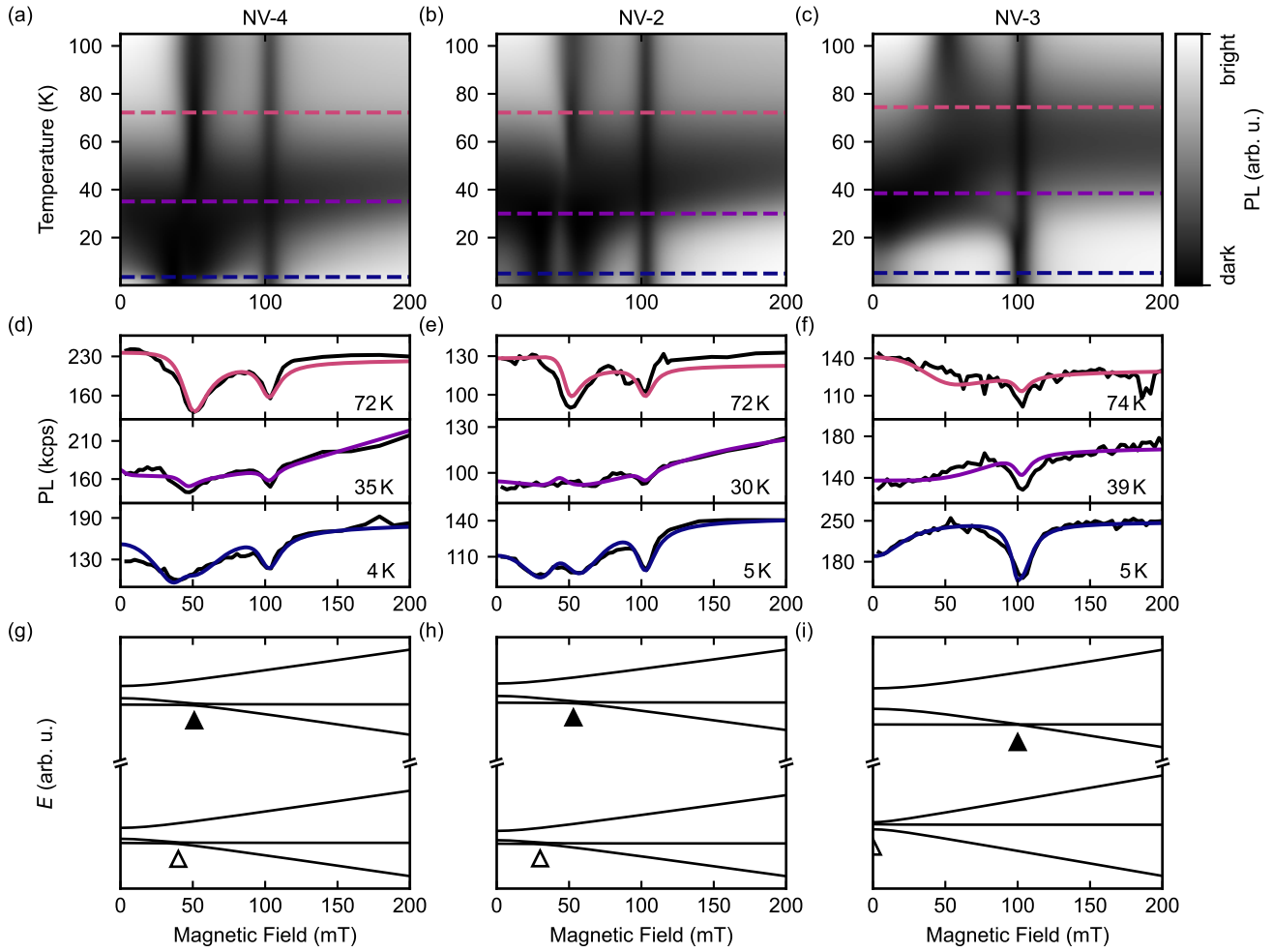

Figure S5. **Temperature dependence of the steady-state PL intensity** - Corresponding to Fig. 3 of the main text. Shown are simulations (a-c), measurements with fits (d-f) and level structures (g-i) for NV-4, NV-2, and NV-3, respectively.

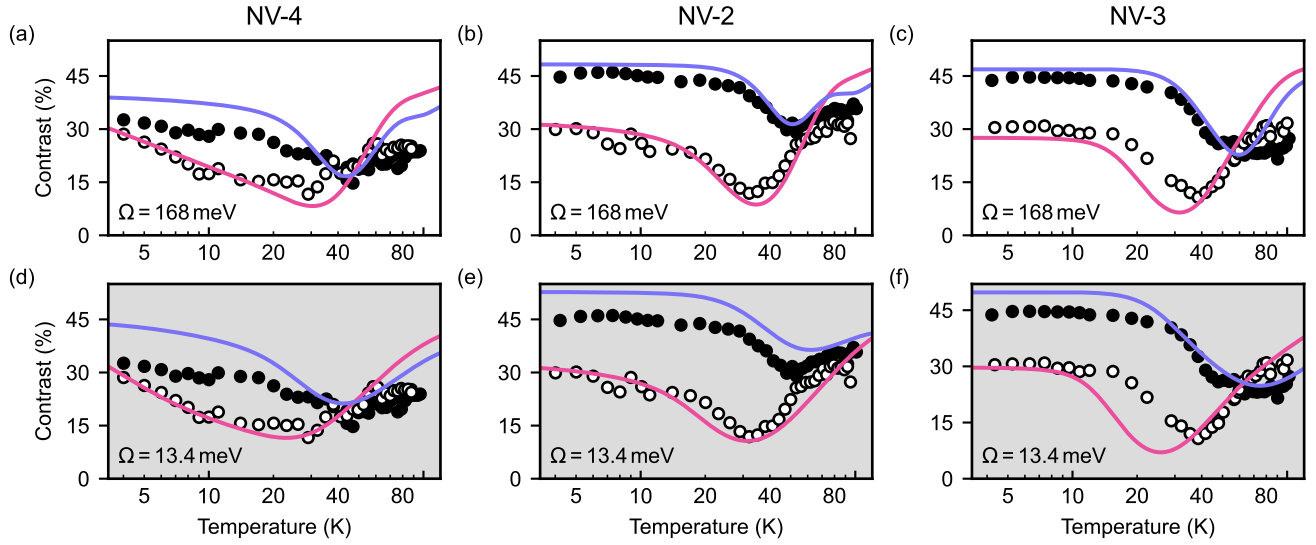

Figure S6. **Comparison between different cut-off energies** - Shown are simulations of temperature-dependent contrast (solid lines) of NV-4, NV-2, and NV-3, with two different phonon cut-off energies Ω. For (a-c) $\Omega_D = 168\,\text{meV}$ as in the main text, for (d-f) $\Omega_P = 13.4\,\text{meV}$ [15]. Empty (filled) circles are the same measurement data taken at 3 mT (200 mT) as presented in Fig. 3(e) of the main text.

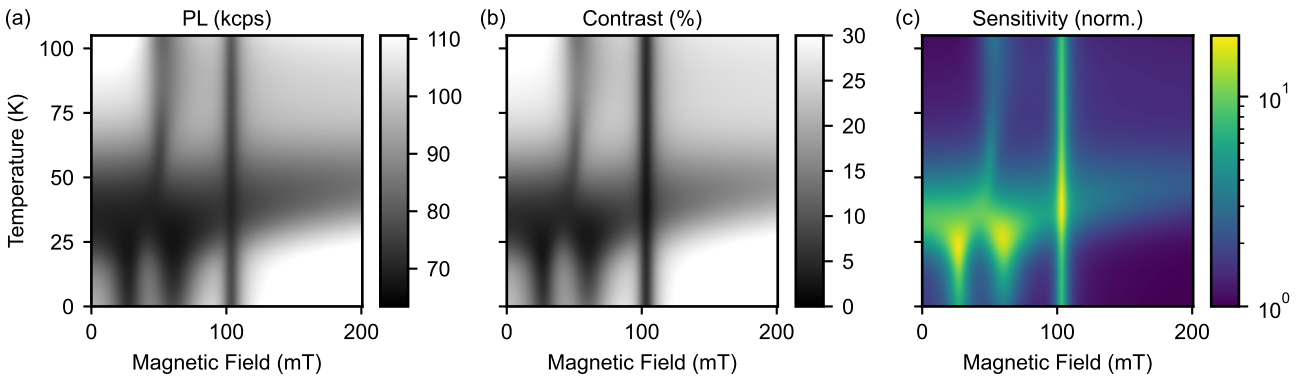

Figure S7. **Comparison of PL, contrast and sensitivity** - Shown are simulated maps of the steady-state PL (a) (same data as Fig. 3(c) of the main text), spin contrast C (b) and normalized sensitivity $s \propto \mathrm{SNR}^{-1}$ (c) for parameters of NV-1. All show qualitatively the same behavior. Since $s \sim (C\sqrt{\mathrm{PL}})^{-1}$, the strong variations in the NV centers sensitivity become apparent when combining (a) and (b), with its vast implications for measurements at intermediate temperatures.

V. ADDITIONAL SIMULATIONS

A. Contrast, PL and sensitivty

In the main text we interchangeably used the PL and the contrast to observe or simulate the temperature dependent photo-physics of the NV center. In Fig. S7(a,b) we give a direct comparison of the temperature and magnetic field dependence of these two observables, demonstrating that they qualitatively show the same behavior. Moreover, in Fig. S7(c) we show the corresponding sensitivity, a measure for the inverse signal-to-noise ratio (SNR) when using the NV center as sensor. In good approximation, it is inversely proportional to the contrast times the square root of the steady-state PL (Eq. S8). Since both quantities are affected significantly by the spin relaxation process discussed in this work, the resulting sensitivity is impaired by more than a factor of 10.

B. Optimal integration time

Since the NV center's photodynamics change with temperature, magnetic field, and strain, the integration time for optimal sensitivity in e.g. a pulsed ODMR measurement also changes. To reduce complexity, we chose to use the same integration time of 250 ns at all conditions. The effect of an integration time optimized for best sensitivity (for details see Eq. S8) at the respective conditions has no influence on the qualitative behavior, as shown in Fig. S8.

C. Spin initialization and readout fidelity

The temperature dependent spin relaxation process discussed in this work affects both, the spin state initialization (by laser illumination) as well as the spin state readout (as e.g. in pulsed ODMRs presented in Fig. 1(a) of the main text). The spin contrast as presented in this work suffers from a combination of both. To illustrate the effect of the spin relaxation process on the initialization and readout individually, we plot them separately in Fig. S9.

D. Extrapolation to low strain or high magnetic field

As discussed in the main text, very high magnetic fields are required to completely suppress the detrimental effect of spin mixing at intermediate temperature. This can be seen in Fig. S10(a) on a map of the NV center sensitivity up to 5 T. Further, the main text claims that the dip in performance at intermediate temperature is common to all NV centers. To that end, we plot in Fig. S10(b) the sensitivity for an NV center that has very low strain, as found in bulk diamond samples. We plot sensitivity instead of PL or spin contrast here, as it is proportional to the inverse SNR

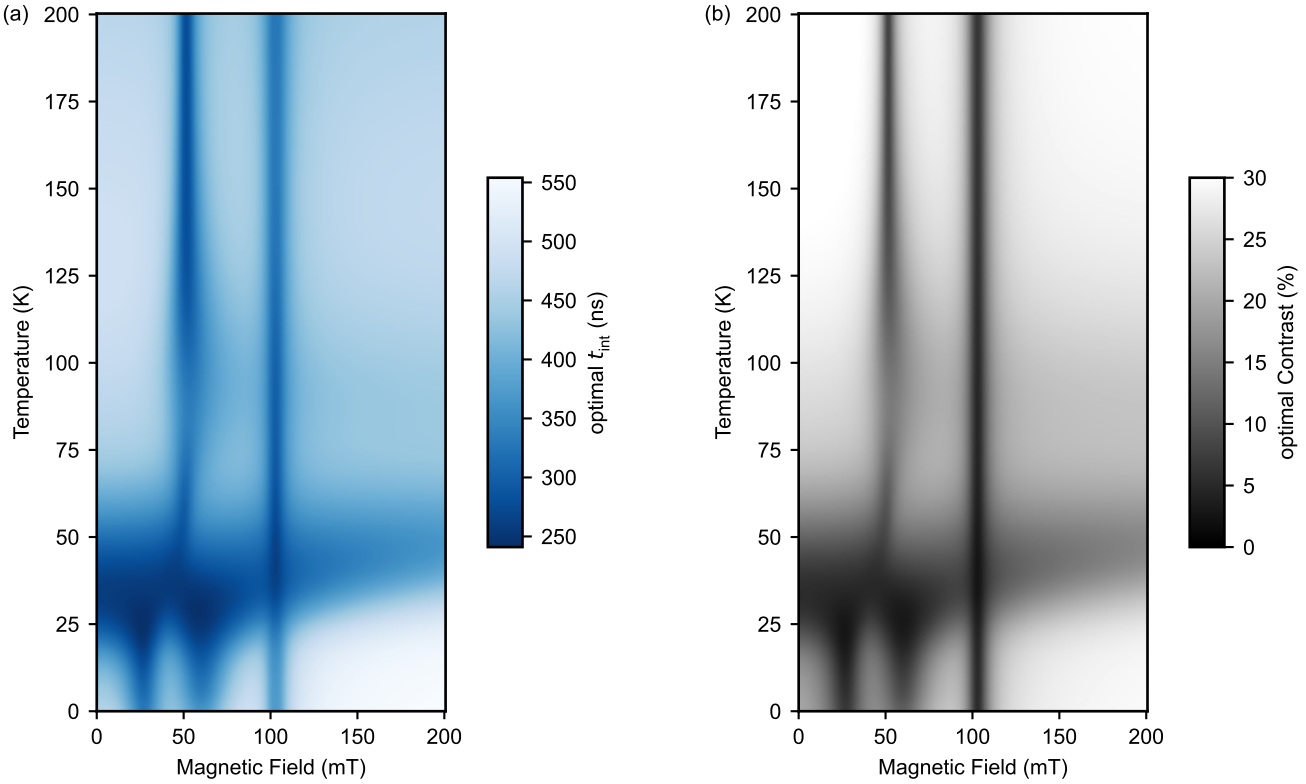

Figure S8. **Optimal integration time for NV-1** - (a) At each field and temperature a simulated pulsed ODMR was optimized for best sensitivity (Eq. S8) and the resulting integration time is plotted. (b) Corresponding spin contrast map. Both maps shows the same pattern as they are dominated by the same spin relaxation process addressed in this work. Spin relaxation in the ES leads to a faster loss of ODMR spin contrast under laser illumination, promoting a shorter integration time. For comparison, the same contrast map for $t_{\mathrm{int}} = 250\,\mathrm{ns}$ is given in Fig. S7(b). While, as expected, a change of t_{int} changes the absolute contrast value, the qualitative behavior is unaffected.

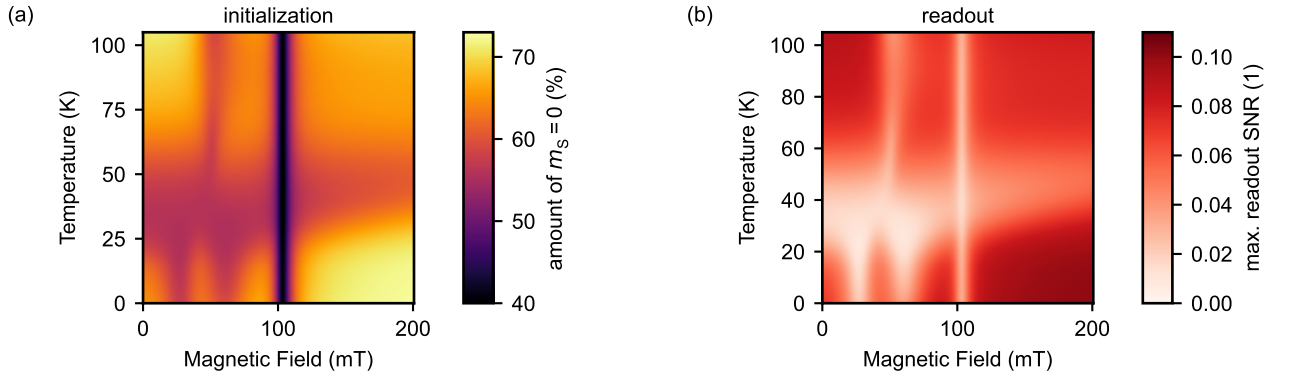

Figure S9. **Effect on spin state initialization and readout** - (a) Simulated map of the amount of $m_{\mathrm{S}} = 0$ after a long green laser pulse followed by a long waiting time (no spin state T_1 process is present). This is a common scheme to initialize the spin state of the NV center. (b) Simulated maximal signal-to-noise ratio of a single spin state readout [9]. For this simulation we assumed a perfect initialization with an amount of $m_{\mathrm{S}} = 0$ of 1. The integration time t_{int} was optimized at each point for maximal signal-to-noise ratio of the readout, which is almost identical to optimizing it for best sensitivity as done in Fig. S8(a) (c.f. Eq. S9). The combination of both (a) and (b) give rise to the reduced performance presented in Fig. S7. Parameters of NV-1 were used.

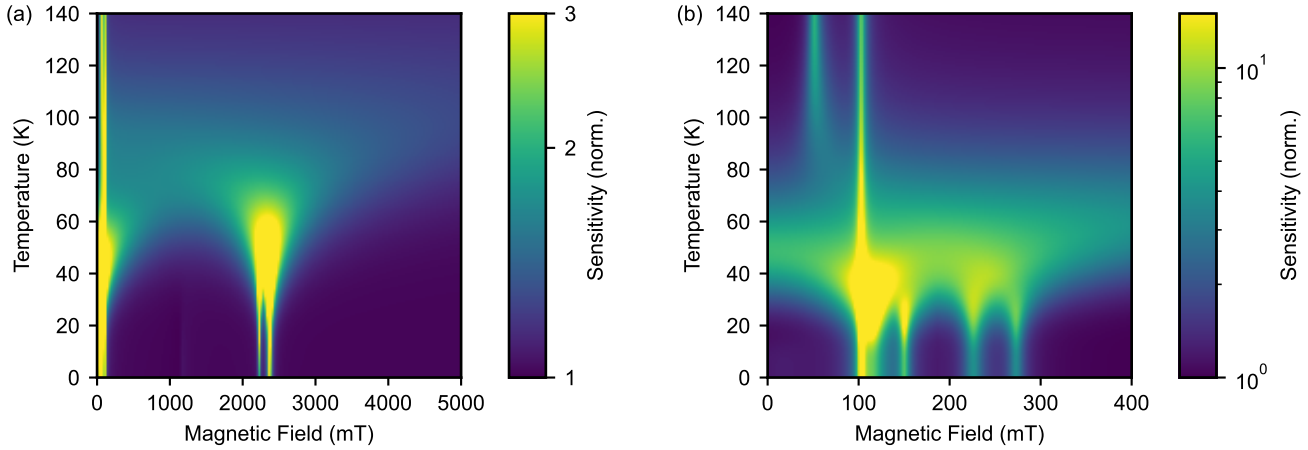

Figure S10. **Model predictions for extreme cases** - (a) Normalized sensitivity map for parameters as found for NV-1 extended to very high magnetic field. Only when approaching $\sim 5\,\mathrm{T}$, the dip in performance at intermediate temperatures gradually disappears. We note though, that this field value is significantly influenced by the position of the LACs above 2 T, which where observed to be shifted to significantly higher fields supposedly due to a strain dependent orbital g_l factor [3]. (b) Normalized sensitivity map for a NV center with very low strain splitting of 1 GHz ($\delta_\perp = 0.5\,\mathrm{GHz}$) as found in bulk diamond. Apart from the strain, parameters are as found for NV-1. The same qualitative behavior is observed as discussed in the main text, though the dip in performance is shifted to higher temperature. For both plots, the integration time was optimized for best sensitivity at each field and temperature for a comparison of performance.

$\lvert\epsilon_{\lvert i\rangle,\lvert j\rangle}\rvert^2$	$\lvert x\rangle\lvert+\rangle$	$\lvert x\rangle\lvert 0\rangle$	$\lvert y\rangle\lvert-\rangle$	$\lvert y\rangle\lvert+\rangle$	$\lvert y\rangle\lvert 0\rangle$
$\lvert x\rangle\lvert-\rangle$	0.	0.003	0.	0.006	0.
$\lvert x\rangle\lvert+\rangle$		0.	0.003	0.	0.
$\lvert x\rangle\lvert 0\rangle$			0.	0.	0.
$\lvert y\rangle\lvert-\rangle$				0.	0.120
$\lvert y\rangle\lvert+\rangle$					0.

Table III. Absolute squares of the spin mixing amplitudes $\lvert\epsilon_{\lvert i\rangle,\lvert j\rangle}\rvert^2$ for the setting of Fig. 2(c) in the main text. Only the $\lvert y\rangle\lvert 0\rangle$ and $\lvert y\rangle\lvert-\rangle$ states mix significantly.

and therefore the relevant quantity when comparing the performance of the NV^- center under different conditions. In section III E, a brief derivation of the sensitivity relation (Eq. S8) used here is provided.

VI. SPIN MIXING AMPLITUDES

In the main text, we introduce the spin mixing amplitude $\epsilon_{|i\rangle,|j\rangle}$ to describe the superposition between two basis states, where one of them contributes only a small amount. In a Bloch sphere picture, this amounts to only a small inclination from one of the poles (where the poles are given by the two basis states) [9]. In this picture, the new eigenstate $|\mathrm{es}\rangle$ is given by

$$|\mathrm{es}\rangle = |i\rangle + \epsilon_{|i\rangle,|j\rangle}\,|j\rangle\ . \tag{S11}$$

The new state $|\mathrm{es}\rangle$ is not properly normalized, but for sufficiently small $\epsilon_{|i\rangle,|j\rangle}$, this is a good approximation of the actual eigenstate $|\tilde{\mathrm{es}}\rangle$. We calculate the $\epsilon_{|i\rangle,|j\rangle}$ by projecting the basis states onto the various eigenstates, such that (for a given eigenstate)

$$\epsilon_{|i\rangle,|j\rangle} = \frac{\langle j|\tilde{\mathrm{es}}\rangle}{\langle i|\tilde{\mathrm{es}}\rangle}\ . \tag{S12}$$

In Tab. III, we give the absolute squares of all relevant $\epsilon_{|i\rangle,|j\rangle}$, given the setting of Fig. 2(c).

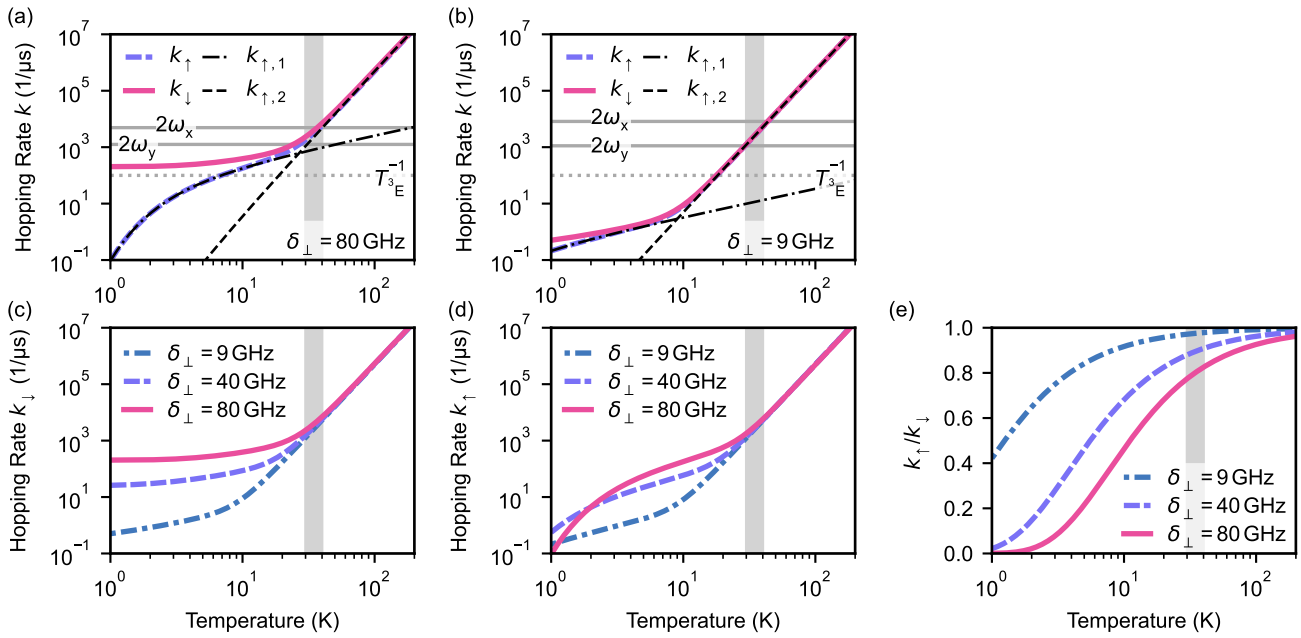

Figure S11. **Orbital hopping rates under different conditions** - (a) Rates up and down and contributions to the up rate of the one- and two-phonon processes for high strain. Also shown are the inverse optical lifetime $T_{^3E}^{-1}$ and twice the Larmor frequencies $2\omega_{x(y)}$ (in MHz) as horizontal lines. Unless specified otherwise, the same setting as in Fig. 2(c) and (d) of the main text is used in the entire figure. The 30 K − 40 K region where highest spin relaxation is observed is marked (gray shading). (b) Same for low strain. In both (a) and (b), the same overlap of the region of highest spin relaxation with the range where twice the Larmor frequencies and rates match is observed as explained for medium strain in the main text. (c) Effect of strain on the hopping rate down. (d) Effect of strain on the hopping rate up. (e) Ratio of rate up and down for different strains.

VII. STRAIN DEPENDENCE OF ORBITAL HOPPING RATES

As the orbital hopping rates – paired with the spin mixing discussed in the main text – cause the observed spin relaxation process, we give a broader overview of their strain dependence here. The temperature dependence of the orbital hopping rates up ($k_\uparrow$) and down ($k_\downarrow$) are plotted in Fig. S11. We use the same parameter set as in Fig. 2(d) of the main text, but vary the in-plane strain $\delta_\perp$. In Fig. S11(a), we present a similar setting as in Fig. 2(d), but for high strain $\delta_\perp = 80$ GHz. In Fig. S11(b) the same setting is also plotted for our low strain case of $\delta_\perp = 9$ GHz.

At high strain in Fig. S11(a), as discussed in the main text, two effects can be observed. First, at low temperature we find a significantly higher $k_\downarrow$ for high strain $\delta_\perp$ (Fig. S11(c)). This is caused by the increase of the phonon mode density with energy. If the orbital branch splitting $\sim 2\delta_\perp$ is larger, a higher mode density is available for the spontaneous one-phonon emission process (c.f. second term in Eq. 1 of the main text). Second, we also find a rapid increase of $k_\uparrow$ at high strain with rising temperature (Fig. S11(d)). At very low temperature and high strain, the phonon modes required for the one-phonon absorption process are not populated. But with rising temperature, they rapidly get thermally activated and $k_\uparrow$ reaches the high value of $k_\downarrow$. This can be seen in the detailed balance of the rates in Fig. S11(e), yielding a Boltzmann distribution of population. This combination of, first, a high $k_\downarrow$ with, second, a rapidly increasing $k_\uparrow$ below 10 K gives rise to the observed drop of spin contrast in Fig. 3(e) of the main text.

* degenc@ethz.ch; †These authors contributed equally.

[1] P. J. Scheidegger, S. Diesch, M. L. Palm, and C. L. Degen, Scanning nitrogen-vacancy magnetometry down to 350 mK, Appl. Phys. Lett. **120**, 224001 (2022).
[2] L. J. Rogers, R. L. Mcmurtrie, M. J. Sellars, and N. B. Manson, Time-averaging within the excited state of the nitrogen-vacancy centre in diamond, New J. Phys. **11**, 063007 (2009).
[3] J. Happacher, D. A. Broadway, J. Bocquel, P. Reiser, A. Jimenéz, M. A. Tschudin, L. Thiel, D. Rohner, M. l. G. Puigibert,

B. Shields, J. R. Maze, V. Jacques, and P. Maletinsky, Low-temperature photophysics of single nitrogen-vacancy centers in diamond, Phys. Rev. Lett. **128**, 177401 (2022).
[4] K. C. Fu, C. Santori, P. E. Barclay, L. J. Rogers, N. B. Manson, and R. G. Beausoleil, Observation of the dynamic Jahn-Teller effect in the excited states of nitrogen-vacancy centers in diamond, Phys. Rev. Lett. **103**, 256404 (2009).
[5] R. Ulbricht, S. Dong, I. Chang, B. M. K. Mariserla, K. M. Dani, K. Hyeon-Deuk, and Z. Loh, Jahn-teller-induced femtosecond electronic depolarization dynamics of the nitrogen-vacancy defect in diamond, Nat. Commun. **7**, 13510 (2016).
[6] D. Wirtitsch, G. Wachter, S. Reisenbauer, M. Gulka, V. Ivády, F. Jelezko, A. Gali, M. Nesladek, and M. Trupke, Exploiting ionization dynamics in the nitrogen vacancy center for rapid, high-contrast spin, and charge state initialization, Phys. Rev. Research **5**, 013014 (2023).
[7] L. Robledo, H. Bernien, T. van der Sar, and R. Hanson, Spin dynamics in the optical cycle of single nitrogen-vacancy centres in diamond, New J. Phys. **13**, 025013 (2011).
[8] N. Manson, J. Harrison, and M. Sellars, Nitrogen-vacancy center in diamond: model of the electronic structure, Phys. Rev. B **74**, 104303 (2006).
[9] S. Ernst, P. J. Scheidegger, S. Diesch, and C. L. Degen, Modeling temperature-dependent population dynamics in the excited state of the nitrogen-vacancy center in diamond, arXiv:2304.02521 (2023).
[10] M. W. Doherty, N. B. Manson, P. Delaney, F. Jelezko, J. Wrachtrup, and L. C. Hollenberg, The nitrogen-vacancy colour centre in diamond, Phys. Rep. **528**, 1 (2013).
[11] S. M. Blakley, T. T. Mai, S. J. Moxim, J. T. Ryan, A. J. Biacchi, A. R. H. Walker, and R. D. McMichael, Spectroscopy of photoionization from the ^{1}E singlet state in nitrogen-vacancy centers in diamond, arXiv:2301.10383 (2023).
[12] M. L. Goldman, A. Sipahigil, M. W. Doherty, N. Y. Yao, S. D. Bennett, M. Markham, D. J. Twitchen, N. B. Manson, A. Kubanek, and M. D. Lukin, Phonon-induced population dynamics and intersystem crossing in nitrogen-vacancy centers, Phys. Rev. Lett. **114**, 145502 (2015).
[13] M. L. Goldman, M. W. Doherty, A. Sipahigil, N. Y. Yao, S. D. Bennett, N. B. Manson, A. Kubanek, and M. D. Lukin, Erratum: State-selective intersystem crossing in nitrogen-vacancy centers [phys. rev. b 91, 165201 (2015)], Phys. Rev. B **96**, 039905 (2017).
[14] A. Gali, Ab initio theory of the nitrogen-vacancy center in diamond, Nanophotonics **8**, 1907 (2019).
[15] T. Plakhotnik, M. W. Doherty, and N. B. Manson, Electron-phonon processes of the nitrogen-vacancy center in diamond, Phys. Rev. B **92**, 081203 (2015).
[16] M. L. Goldman, M. W. Doherty, A. Sipahigil, N. Y. Yao, S. D. Bennett, N. B. Manson, A. Kubanek, and M. D. Lukin, State-selective intersystem crossing in nitrogen-vacancy centers, Phys. Rev. B **91**, 165201 (2015).
[17] A. Dreau, M. Lesik, L. Rondin, P. Spinicelli, O. Arcizet, J. F. Roch, and V. Jacques, Avoiding power broadening in optically detected magnetic resonance of single NV defects for enhanced dc magnetic field sensitivity, Phys. Rev. B **84**, 195204 (2011).
[18] D. A. Hopper, H. J. Shulevitz, and L. C. Bassett, Spin readout techniques of the nitrogen-vacancy center in diamond, Micromachines **9**, 437 (2018).
[19] L. C. Bassett, F. J. Heremans, D. J. Christle, C. G. Yale, G. Burkard, B. B. Buckley, and D. D. Awschalom, Ultrafast optical control of orbital and spin dynamics in a solid-state defect, Science **345**, 1333 (2014).
[20] X. D. Chen, C. H. Dong, F. W. Sun, C. L. Zou, J. M. Cui, Z. F. Han, and G. C. Guo, Temperature dependent energy level shifts of nitrogen-vacancy centers in diamond, Appl. Phys. Lett. **99**, 161903 (2011).
[21] J. Tetienne, L. Rondin, P. Spinicelli, M. Chipaux, T. Debuisschert, J. Roch, and V. Jacques, Magnetic-field-dependent photodynamics of single NV defects in diamond: an application to qualitative all-optical magnetic imaging, New J. Phys. **14**, 103033 (2012).
[22] A. Gupta, L. Hacquebard, and L. Childress, Efficient signal processing for time-resolved fluorescence detection of nitrogen-vacancy spins in diamond, J. Opt. Soc. Am. B **33**, B28 (2016).
[23] N. Kalb, P. C. Humphreys, J. J. Slim, and R. Hanson, Dephasing mechanisms of diamond-based nuclear-spin memories for quantum networks, Phys. Rev. A **97**, 062330 (2018).
[24] T. A. Abtew, Y. Y. Sun, B. Shih, P. Dev, S. B. Zhang, and P. Zhang, Dynamic Jahn-Teller effect in the NV^- center in diamond, Phys. Rev. Lett. **107**, 146403 (2011).